J Mater Sci: Mater Electron **(2023) 34:2028**

Structural characterizations and electrochemical performances of rGO-based anode materials for lithium-ion battery

Nur Ezyanie Safie[1,3], Mohd Asyadi Azam[1,2,*], Chun Khean Chiew[1], Mohd Fareezuan Abdul Aziz[4], Mohamad Nazmi Faiz Md Sairi[1], and Akito Takasaki[5]

[1] Fakulti Teknologi Dan Kejuruteraan Industri Dan Pembuatan, Universiti Teknikal Malaysia Melaka, Hang Tuah Jaya, 76100 Durian Tunggal, Melaka, Malaysia
[2] Centre for Promotion of Educational Innovation, Shibaura Institute of Technology, 3-7-5 Toyosu, Koto-Ku, Tokyo 135-8548, Japan
[3] Fakulti Teknologi Dan Kejuruteraan Elektrik, Universiti Teknikal Malaysia Melaka, Hang Tuah Jaya, 76100 Durian Tunggal, Melaka, Malaysia
[4] School of Physics, Universiti Sains Malaysia, USM, 11800 Penang, Malaysia
[5] Department of Engineering Science and Mechanics, Shibaura Institute of Technology, 3-7-5 Toyosu, Koto-Ku, Tokyo 135-8548, Japan

Received: 15 July 2023
Accepted: 26 September 2023

ABSTRACT

Lithium-ion batteries (LIBs) in the current market are becoming insufficient to meet the increasing demand for portable electronic devices and large-scale applications due to the low theoretical capacity (372 mAh/g) and poor rate performance of the graphite anode. This work focuses on electrochemical performance analysis using graphene as an active material in constructing an anode for LIB. Graphene has been used in the form of reduced graphene oxide (rGO) because it can be produced using more scalable and cost-effective techniques. Three graphene samples were tested, including synthesized rGO, industrial graphene, and commercial rGO. Raman spectroscopy confirms the successful reduction of rGO by chemical synthesis and shows that the commercial rGO has the fewest defects among the three graphene samples. XRD characterization shows that chemically synthesized rGO has a more crystallized structure and larger d-spacing; Meanwhile, electrochemical analysis showed that the commercial rGO performs better, including cyclic stability. The first discharge capacity is 2383 mAh/g with a high current density of 100 mA/g. The commercial rGO delivers an energy density of up to 1866 Wh/kg, demonstrating the potential to produce compact, high energy density batteries for electronic devices, electric cars and power grid storage applications.

Address correspondence to E-mail: asyadi@utem.edu.my

https://doi.org/10.1007/s10854-023-11398-3

1 Introduction

Power generation and energy storage systems are extremely challenging technologies in this century to overcome the imminent depletion of fossil fuels [1–3]. Lithium-ion batteries (LIBs) with remarkable power and energy densities and extended lifetimes are essential for the development of portable devices, electric vehicles, and power grid storage. However, current LIBs cannot meet this need because they mainly use graphite as an anode, which has a low capacity of 372 mAh/g and thus a low power rate [4]. The problem of lithium deposition is always present in conventional fast-charging lithium-ion batteries with graphite anodes, shortening lifespan and raising serious safety concerns [5]. Among the many challenges of applying graphite anodes for LIB are their limited rate capability, especially for the lithiation process (full cell charge), and the risk of lithium metal coating on the electrode surface, which could lead to cell short-circuit or at least, rapid ageing and accelerated cell fading [6].

Also, graphite can only form stoichiometric LiC_6 by intercalating only one lithium-ion for every six carbon atoms, resulting in a low capacity anode for lithium-ion batteries. In addition, batteries with graphite anodes often only have a moderate power density since lithium ions diffuse relatively slowly in carbon materials (between 10^{-12} and 10^{-6} cm^2/s). The slow diffusion rate also affects the discharge and charge rate of the LIBs and limits the maximum power output and input of the lithium-ion batteries. Moreover, owing to the continuous volume changes and the development of lithium dendrites, graphite-based anodes are prone to delamination and mechanical fracture during cycling, which affects the cyclic performance of the battery [7].

In a battery, capacity represents-specific energy in ampere-hours (Ah). Ah is the discharge current that a battery can deliver over a period of time. The gravimetric energy density or capacity or specific energy of a battery is a measure of how much energy a battery contains compared to its weight and is usually expressed in watt-hours/kilogram (Whr/kg). On the other hand, the volumetric (area) capacitance values are calculated based on the total volume (area) of the electrode film. Volumetric energy density refers to the amount of energy that can be contained in a given volume. The volumetric energy density of batteries, for example, allows electric vehicles to travel further without increasing the size of the battery pack.

Han et al. [8] claimed theoretically, the graphite anode of LIBs is not stable since its operating voltage is approximately 0.05 V, which is outside the stabilised voltage window of a general liquid organic electrolyte, which is roughly 1–4.5 V. Besides, during the charge and discharge processes, Li-ion consumption and electrolyte breakdown occur, resulting in the formation of a protective layer on the graphite anode electrode surface known as Solid Electrolyte Interface (SEI) film. The SEI film will continue to form and thicken, reducing the battery's usable capacity and increasing the internal resistance of the battery. Asenbauer et al. [6] claimed that the primary problems for graphite anodes in Li-ion batteries are their restricted rate capability, particularly during the cell charging, and the danger of lithium metal plating on the electrode surface, which can result in cell short-circuiting, raping ageing, and rapid cell fading. Besides the poor rate capability, graphite-based anodes also suffer irreversible first cycle capacity caused by reductive electrolyte breakdown, which results in Li^+ consumption as the charge carrier.

Moreover, KumarMarka et al. [9] added that in order to compensate, more Li^+ must be added to the positive electrode, which increases the cell's weight, raises fabrication costs, and reduces the positive electrode's capacity. According to Lu et al. [10], the ideal anode for LIBs should have the attributes of high reversible capacity, low potential versus opposing electrode, extended life, cheap cost, great tolerance for abusive use, environmentally friendly, and high-rate capability. However, graphite possesses poor capacity at 372 mAh/g because it only enables one lithium atom to be intercalated for every six carbon atoms, producing a stoichiometric LiC_6. Furthermore, since lithium-ion diffuses into carbon materials at a low rate; typically, from 10^{-12} to 10^{-6} cm^2/s, batteries with graphite anodes generally have a moderate power density.

The graphene-based devices have become a reality and have evolved into advanced technologies [11, 12]. The unique two-dimensional structure and exceptional properties of graphene make it superior to other carbonaceous materials in rapid surface absorption, diffusion, and electron transport of lithium ions. The reduced graphene oxide (rGO) possesses unique properties that make it a promising anode material for batteries. Its high specific surface area allows for increased electrode–electrolyte interaction, facilitating higher lithium-ion storage capacity. The two-dimensional structure of rGO sheets provides efficient pathways for lithium-ion diffusion, enhancing the electrode's rate capability. Additionally, rGO exhibits excellent electrical conductivity, ensuring rapid electron transport during charge and discharge cycles, and contributing to improved overall battery performance. Moreover, the flexibility and mechanical robustness of rGO sheets mitigates the stress associated with volume expansion and contraction during lithium-ion intercalation, enhancing the anode's durability and cyclability. These attributes make rGO an attractive choice for next-generation lithium-ion batteries, offering a balance between energy storage capacity, cycle life, and rate performance, and paving the way for advancements in sustainable energy storage technologies.

The problem statement of this work is identified starting from the main problem of poor performance and durability of typical LIBs. It is narrowed down to the limitation of the graphite-based anode in the LIBs. However, the techniques for making graphene are still at an immature stage and prohibitively expensive. The structural properties of graphene depend on the manufacturing conditions and processing equipment, resulting in poor controllability on an industrial scale [13]. Therefore, this study focuses on the use of graphene derivative, rGO which is well-known to be cost-effectively produced, as an anode in LIBs. rGO was selected from different productions which shows the uniqueness of this material depending on its production background. The significance of the study highlights the potential of an rGO-based anode to improve the performance and durability of LIBs, thereby contributing to the development of portable energy storage technology.

2 Materials and methods

2.1 Descriptions of all graphene samples used in this study

In this study, three different graphene derivatives were used as anode material, referred to synthesized rGO, commercial rGO, and industry's graphene. Synthesized rGO was synthesized using the chemical synthesis technique based on the modified Hummer's method as described in our previous work [14]. On the other hand, the Industry's graphene is derived from agricultural waste, specifically sourced from palm kernel shells. These shells, a byproduct of the palm oil industry, present a sustainable and environmentally responsible source for graphene production. The initial raw material, palm kernel shells, undergoes a series of carefully designed processes, including pyrolysis and high-temperature treatments. These thermal processes transform the organic waste into graphite, a crystalline carbon form, which is then further refined to obtain high-quality graphene. The controlled and high-temperature treatments are critical in achieving the desired structure and properties necessary for effective graphene integration in a variety of industrial applications. It was produced by a start-up company in Malaysia and due to the policy issue, the company's name has to be kept secret. Also, the Commercial rGO was developed by a China-based company called Luoyang Tongrun Nano Technology Co., Ltd. (or TRUNNANO) with product number TR2021012708.

2.2 Graphene anode materials characterization

Analysis of Raman spectra of carbon materials is an excellent approach to detect graphitic carbon (G-band) and disordered carbon (D-band). Raman spectra were recorded with a laser excitation of 514 nm (Nd-YAG; green laser) with a power of 50 mW and an exposure time of 10 s. The obtained Raman spectra were used to confirm the structural properties of the graphene samples by examining the D- and G-band peaks. The peak can be influenced by the bonding between the atoms with the G-band due to the in-plane vibrations of bonded carbon atoms and the D-band corresponding to the presence of structural defects induced by the out-of-plane vibrations. The I_D/I_G ratio of intensities represents the defects, including edges, voids, and ripples, which are used to assess the quality of the anode material. The I_{2D}/I_G ratio, on the other hand, is beneficial in determining the number of layers in the rGO. The G-band typically reflects the character of the graphitic carbon corresponding to sp^2 bonding, while the D-band is beneficial for detecting defects, edge sites, and pores in graphene [15, 16].

The scanning electron microscope (SEM), Zeiss EVO 50 XVP, was used to examine the morphological properties of the graphene samples. The magnified images of graphene samples are useful for studying the changes in a morphological structure, such as the layered structure and nanosheet profiles. The electron acceleration voltage used for the SEM analysis on the rGO is 10 kV. The crystalline structures of the graphene samples were assessed by X-ray diffraction

(XRD) analysis, revealing chemical composition information. The X-ray source was Cu-Kα radiation with a wavelength of 1.5406 Å. The results were collected between scattering angles (2θ) of 10°–90°. A diffraction peak at 2θ in the graphene samples produced an XRD pattern that was examined to identify the arrangement of the crystalline phase [17]. Also, the XRD pattern used to evaluate the distance between the layers matched the width of the peak in the XRD pattern to confirm the successful removal of the oxygen-containing functional groups by the reduction process.

2.3 Cell preparation

In general, the half-cells were fabricated through five main processes, namely mixing, coating, drying, stamping, and assembling to produce the working electrode prior to the half-cell assembly process. Three graphene samples are used as the anode material including synthesized rGO, industrial graphene, and commercial rGO. The working electrodes were constructed by blending the active material with acetylene black (AB) and polyvinylidene fluoride (PVDF) in a weight ratio of 80:10:10. The AB was added as a conductive agent while the PVDF was used as a binder. Manual electrode fabrication and coin cell assembly were utilized to fabricate the CR-2032 graphene anode half-cell. The homogeneous slurry mixture was first prepared before being applied to the copper foil using the film and adjustable applicator. Then the coated copper foil was oven-dried before being stamped prior to assembly of the half-cell.

The copper foil used in this work is commercially available, made in Japan, type C1100R-H, 15–20 microns thick. The copper foil stability and the electrochemical voltage window of a LIB system correlate directly with the electrolyte used. The electrolyte used is the commercial LIB electrolyte which is 1 M $LiPF_6$. Most commercial LIBs use similar copper foil in the anode (mostly graphite), regardless of the carbon-based anode material. It is very common that this electrolytic anode system can withstand a window of up to 3.7 or even 4.0 V. Copper foil in a LIB system is very stable and does not reflect copper's Pourbaix system, which only shows the plot of the equilibrium potential of electrochemical reactions versus pH. It shows how corrosion mechanisms can be studied as a function of factors such as pH, temperature, and the concentrations of reacting species. So, as long as there is no drastic temperature change, there is no need to worry about the stability of the copper foil.

The mixture of active material, AB and PVDF was prepared as a slurry in N-methyl pyrrolidone (NMP) solvent during the mixing process. Several mixing methods and parameters were tested to prepare the slurry for electrode preparation. The best method for preparing the most homogeneous slurry adopted for this project started with NMP at approximately 1.93 g and heated to 80 °C while stirring with a magnetic stirrer; the beaker was sealed with parafilm/foil to prevent NMP from evaporating. Based on our limited knowledge, the ratio of the NMP depends on the physical properties of the sample and needs to be as low as possible. PVDF was gradually added to the heated NMP with stirring. Once PVDF was dissolved (transparent yellowish color), the temperature was lowered to 60 °C with stirring. Active material and acetylene black were gradually added while stirring at 60 °C. Once the mixture was homogenous, the viscosity of the mixture was adjusted by increasing the viscosity and continued stirring while heating to 60 °C without sealing the beaker to allow excess NMP to evaporate. Once the desired viscosity was reached, the beaker was removed from the magnetic stirrer and sealed with parafilm to prevent further evaporation.

The coating of the slurry on the current collector (copper foil) was performed using the film applicator and holder. The thickness used to apply the slurry to the copper foil was set at 0.65 mm using an adjustable applicator. The electrode slurry coated copper foil was then dried using an oven at 100 °C for 12 h to allow the NMP solvent to fully evaporate from the coated slurry and to ensure the rest of the mixture was properly adhered and attached to the copper foil current collector for the following process. After drying, the electrode was removed from the oven and punched into discs with a diameter of 17 mm using the hand punch tool for. The 20 mm diameter CR2032 coin cell components were used for the half-cell assembly process. The cells for all three graphene samples were assembled in the argon-filled glovebox with seven components, as shown in Fig. 1.

The coin cell base was positioned up with a flat side down. 2 drops of lithium hexafluorophosphate ($LiPF_6$) electrolyte was dropped into the coin cell base cup, and the working electrode (graphene anode) was placed on top. The electrolyte was a commercially available electrolyte, namely an EC/EMC/DEC + VC + other additive 1 M $LiPF_6$. Another 3 drops

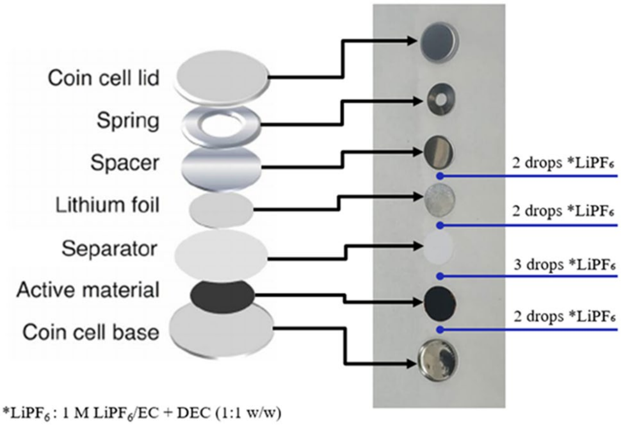

*$LiPF_6$: 1 M $LiPF_6$/EC + DEC (1:1 w/w)

Fig. 1 The construction of coin cell 2032 components

of $LiPF_6$ electrolyte were added to the surface of the working electrode before the separator was placed on top. Next, another 2 drops of $LiPF_6$ electrolyte were dripped onto the separator before the lithium foil disc counter electrode was placed onto the separator. Then the stainless-steel spacer was placed on top of the lithium foil, followed by the spring and the coin cell lid. The hydraulic crimping machine was then used to crimp the coin cell at a pressure of 100 kg/cm^2. The assembled cells were stored overnight (at least 12 h) in a glass container to soak before evaluating electrochemical suitability. It is critical to ensure that the separator fully covers the surface of the working electrode to prevent internal short-circuit of the assembled cells. Proper and sufficient crimping pressure is vital to prevent the working electrode and lithium foil from reacting with the outer atmosphere and to avoid cell rupture due to swelling of the anode and lithium foil after reaction with the $LiPF_6$ electrolyte.

2.4 Electrochemical evaluation

The assembled cells were soaked overnight prior to electrochemical testing. The assembled cells were subjected to galvanostatic charge and discharge cycling at a voltage window of 0.01 and 3.00 V (vs. Li/Li$^+$). Cyclic voltammetry (CV) was performed over the potential range of 0.01–3.00 V at a scan rate of 0.2 mV/s. The assembled cells were also cycled for 70 cycles at a current density of 100 mA/g under the voltage window of 0.01 to 3.00 V. All tests were performed using the potentiostat/galvanostat at room temperature. The results of the electrochemical performance testing, such as the discharge/charge profiles, capacities versus cycle number, CV, and cyclic performance, were used to determine the specific capacity, charge–discharge cyclic stability, and energy density of the graphene anodes.

The specific capacity was calculated from the plotted discharge/charge profiles resulting from the galvanostatic discharge/charge evaluation. The data from the initial plot then extracts the final discharge/charge profiles of the graphene anode, where the x-axis is the specific capacity (mAh/g) and the y-axis is voltage (V). The Coulombic efficiency is crucial to determine the ability of the graphene anode to reverse the discharge–charge capacity in each cycle and to verify the presence and magnitude of the electrochemical side reactions during each cycle. The Coulombic efficiency of the 1st (initial) cycle and the 10th cycle is calculated by the following equation:

$$\text{Coloumbic efficiency}\,(\%) = \frac{\text{Charge capcity}_{(n)}}{\text{Discharge capacity}_{(n)}} \times 100 \tag{1}$$

where: n = cycle number or cycle n.

The cyclic stability of the graphene anode is determined by the cycling performance graph. The initial graph of the cyclic performance of the graphene anode half-cell has been plotted by taking the recorded discharge–charge capacity after each cycle. Then the final graph was plotted with the x-axis of cycle number and y-axis of specific capacity (mAh/g). The cycling performance graph analyzes the cycling stability by examining the cycling trends of the graphene anode. The capacity retention is then calculated to determine the percentage of capacity retained or loss of capacity from the first discharge capacity at 10 cycles after the first cycle. Capacity retention is essential to verify the long-term cycle life and durability of the graphene anode in the LIB application. The capacity retention is calculated using the following equation:

$$\text{Capacity retention}\,(\%) = \frac{\text{Discharge capacity}_{(n)}}{\text{Discharge capacity}_{(i)}} \times 100, \tag{2}$$

where: n = cycle number of cycle n, and i = initial or first cycle.

The energy density graphs were generated by WonATech Smart Interface, according to the energy discharged or charged during each cycle. The recorded discharge and charge energy density data were plotted on the final graphs, with the X-axis representing cycle number and the Y-axis representing energy density (Wh/kg). The energy density graph evaluated the potential of the graphene anode to store the maximum and minimum discharge and charge energy during the 70-cycle test. The energy density is also calculated by Eq. (3) as follows:

$$\text{Energy density (Wh/kg)} = \text{Nominal voltage}\,(V) \times \frac{\text{Anode capacity (Ah)}}{\text{Anode weight (kg)}}, \tag{3}$$

where nominal voltage = average or midpoint operating voltage, and anode capacity = capacity obtained from the cyclic stability.

The C-rate was calculated to determine the discharge or charge rate of the graphene anode half-cell based on the capacity obtained during the cycling performance evaluation. The capacity was taken from the cycling performance data, while the discharge current was taken from the current density used to conduct the test. The C-rate was calculated via the following equation:

$$\text{Discharge current}\,(A) = C - \text{rate}\,(C) \times \text{Capacity}\,(Ah) \tag{4}$$

3 Results and discussion

3.1 Structural characterizations of graphene anode materials

Figure 2 shows that the Raman spectra of the synthesized rGO record a peak position at a Raman shift of 1584 cm^{-1} and 1347 cm^{-1}, while the industry's graphene peak position is at 1592 cm^{-1} and 1348 cm^{-1}. For commercial rGO, the peak position is recorded at a Raman shift of 1589 cm^{-1} and 1363 cm^{-1}. It is observed that the Raman spectra of all three graphene samples have two prominent peaks at a Raman shift of ~ 1580 cm^{-1} and ~ 1350 cm^{-1}, corresponding to G-band and D-band, respectively. The G-band (~ 1580 cm^{-1}) is assigned to first-order scattering of the E_{2g} phonon off the sp^2 carbon–carbon bond. The E_{2g} mode is a doubly degenerate Raman active optical vibration mode in which the carbon atoms move in the graphene plane, confirming the successful synthesis of rGO for synthesized rGO samples and the presence of graphene in industry's graphene and commercial rGO samples [18]. The D-band (~ 1350 cm^{-1}) corresponds to defect sites associated with vacancies and grain boundaries [19]. The information from the Raman spectra is further extracted and is presented in Table 1. The integrated intensity was calculated for the I_D/I_G ratio of each sample. The higher value of the I_D/I_G ratio is associated with an increased defect density due to more elastic scattering. The calculated I_D/I_G ratio shows that the commercial rGO has the lowest defect density among all three samples, followed by the industry's graphene and the synthesized rGO with the highest defect density.

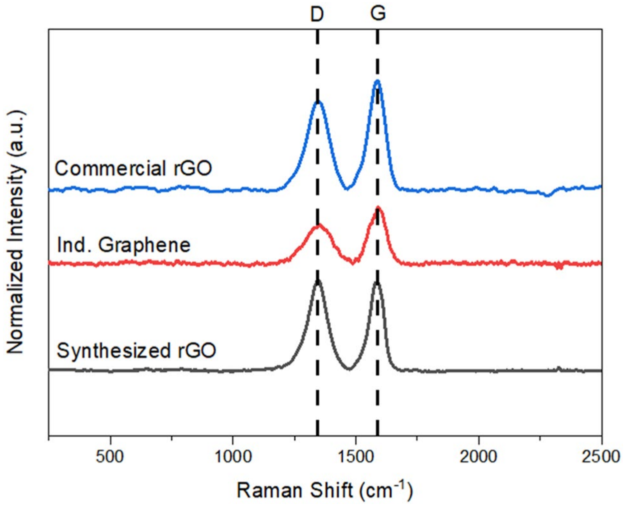

Fig. 2 Raman spectra of synthesized rGO, industry's graphene, and commercial rGO

The morphological structures of all samples were examined by conventional scanning electron microscopy (SEM). The SEM images of the synthesized rGO, the commercial rGO, and the industry's graphene, are shown in Fig. 3. The SEM images of the synthesized rGO showed the formation of wrinkles and folds on the surface of the rGO. Figure 3a shows the crumpled configuration of rGO, which resembles a paper ball-like structure, resulting from thermal reduction and isotropic compression during the chemical synthesis process. Upon exposure of the graphite suspension to heat, isotropic compression occurred, which induced equal stresses in all directions toward the center of the graphite during the thermal reduction process [20]. Figure 3b shows wrinkling on the graphite surface caused by negative thermal expansion rGO is due to graphene's negative coefficient of thermal expansion (TEC) properties,

Table 1 Raman spectra information of all graphene samples

Sample	Peak position (cm^{-1})		Intensity (a.u.)		Integrated intensity		I_D/I_G ratio
	D-band	G-band	D-band	G-band	D-band	G-band	
Synthesized rGO	1347	1584	5628	5593	332,059.46	232,921.07	1.43
Industry's graphene	1348	1592	430	472	42,960.15	41,202.48	1.04
Commercial rGO	1363	1589	934	1035	14,308.43	14,566.01	0.98

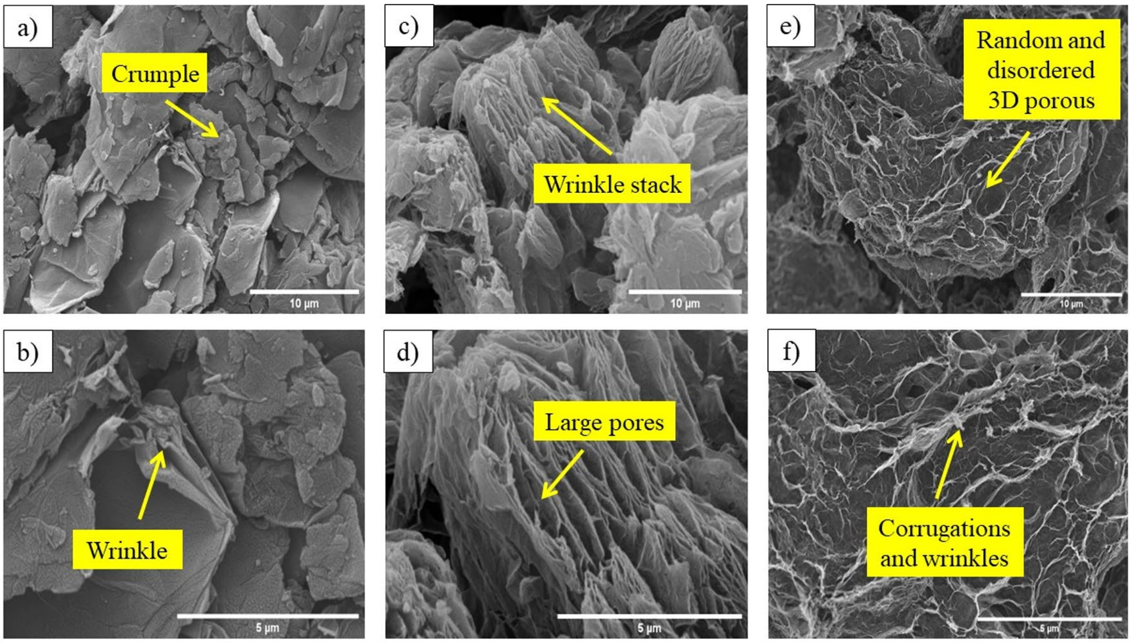

Fig. 3 SEM images of synthesized rGO at **a** 3000× and **b** 10,000× magnification levels, commercial rGO at **c** 3000× and **d** 10,000× magnification levels, and industry's graphene at **e** 5000× and **f** 10,000× magnification levels

where it contracts when heated [21]. Graphene's out-of-plane transverse acoustic mode (ZA) is responsible for the negative thermal expansion [22].

At the same time, this planar 3-coordination is the possible factor of negative expansion in graphene layers [23]. Figure 3e shows the FESEM images of the industry's graphene, in which random and disordered three-dimensional porous architectures can be formed on the industry's graphene surfaces [24]. The disordered porosities are accompanied by a large number of corrugations and wrinkles on the surface of the graphene, as shown in the 10,000 × FESEM images in Fig. 3f, which are most likely caused by a very high-temperature synthesis process. The commercial rGO, on the other hand, features a highly wrinkled structured stack of ultra-thin graphene oxide nanosheets with porous morphology as shown in Fig. 3c [25], possibly indicating an effective exfoliation process during the graphene synthesis process, by thermal exfoliation. Figure 3d also illustrates the observation of large pores between the nanosheets in the commercial rGO. The presence of an extensive porous network is an important feature of electrode materials to promote uniform electrolyte diffusion, and a large specific surface area increases the number of active sites for redox reactions [26].

The resulting XRD patterns for the graphene samples are shown in Fig. 4. Observation of the XRD pattern of all three graphene samples reveals the presence of two prominent peaks at orientations (002) and (100). All samples show a clear peak at (002) plane at 2θ angles of 24.3°, 24.6°, and 24.4° for synthesized rGO, industry's graphene, and commercial rGO, respectively. At (100), the synthesized rGO shows a

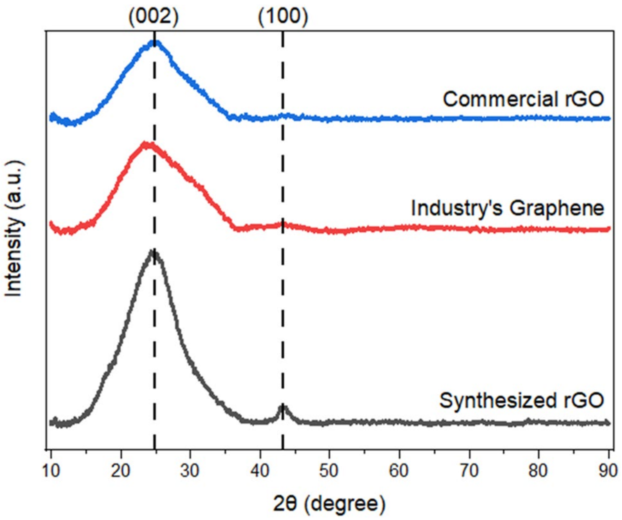

Fig. 4 XRD pattern of synthesized rGO, industry's graphene, and commercial rGO

Table 2 XRD information of all graphene samples based on different important features

Features	Synthesized rGO	Industry's graphene	Commercial rGO
002 (°)	24.30	24.60	24.40
100 (°)	43.30	43.00	43.00
Centroid 002 (°)	24.81	25.30	25.12
FWHM 002	8.28	11.44	9.63
d-Spacing (Å)	3.58	3.52	3.54

prominent peak at a 2θ angle of 43.3°, while the industry's graphene and commercial rGO show a smaller peak at a 2θ angle of 43.0°. The broader peak at (002) orientation at a 2θ angle of ~ 24°–25° indicated that the (002) crystal phase was more randomly arranged (more amorphous, lower crystallization structure) and corresponded to the removal of oxygen-containing functional groups. The less intense peak at (100) from 2θ ~ 42.60° showed the disordered carbon materials band [27]. The synthesized rGO with a more intense peak at (100) showed a less disordered band of the carbon materials than the industry's graphene and commercial rGO.

Additional information was extracted from the XRD pattern of the graphene samples and is presented in Table 2. The centroid and full-width at half maximum (FWHM) values of (002) for all three graphene samples were analyzed and calculated. Comparing the FWHM value of the graphene samples, it is found that the industry's graphene has the broadest peak at (002); Therefore, its crystal phase is arranged rather randomly, followed by commercial rGO while synthesized rGO exhibits the highest crystallized crystal phase among all three samples. In addition, the d-spacing for all graphene samples was also calculated using Bragg's law with the equation $n\lambda = 2d\sin\theta$, where n = integer, λ = wavelength of the X-ray (Å), d = spacing of the crystal layers (Å), and θ = incident angle (°). Using the centroid value at (002) as 2θ in Bragg's law, it is found that industry's graphene has the lowest d-spacing of 3.52 Å, followed by commercial rGO with a d-spacing of 3.54 Å and synthesized rGO with the highest d-spacing of 3.58 Å.

3.2 Electrochemical performance evaluation

3.2.1 *Synthesized rGO*

The electrochemical performances of the samples were evaluated using the potentiostat/galvanostat. Three main tests were performed to evaluate the performance of the graphene samples as an anode material in the LIB, including cyclic voltammetry (CV) measurement, galvanostatic charge–discharge, and anode cyclic (Fig. 5). The CV curves of the synthesized rGO were obtained at a scan rate of 0.2 mV/s and a potential window from 0.01 to 3.00 V versus a Li/Li + reference electrode as shown in Fig. 5a. It was observed that the curve for the first cycle is differs significantly from that of the second and third cycles. A large irreversible reduction current resulting from irreversible lithium-ion intercalation can be observed between the first and subsequent cycles. In the first cathodic scan, a reduction peak at 0.01 V can be observed during the first cycle, which corresponds to the formation of the solid electrolyte interface (SEI) on the surface of the active material and the side reaction of lithium ions with the oxygen-containing groups from graphene sheet [28]. The first anodic scan shows a broad oxidation peak at 1.7 V. The reduction peak can be observed at 0.2 V for the second cathodic scan, which remains almost the same for the third consecutive cycle, indicating that the reversibility of the lithium-ion intercalation was stable after going through the first cycle [29]. The second and third cycles anodic scan shows a consistent oxidation peak with the initial cycle at 1.7 V, corresponding to the oxidation of graphene components reacting with the $LiPF_6$ electrolyte.

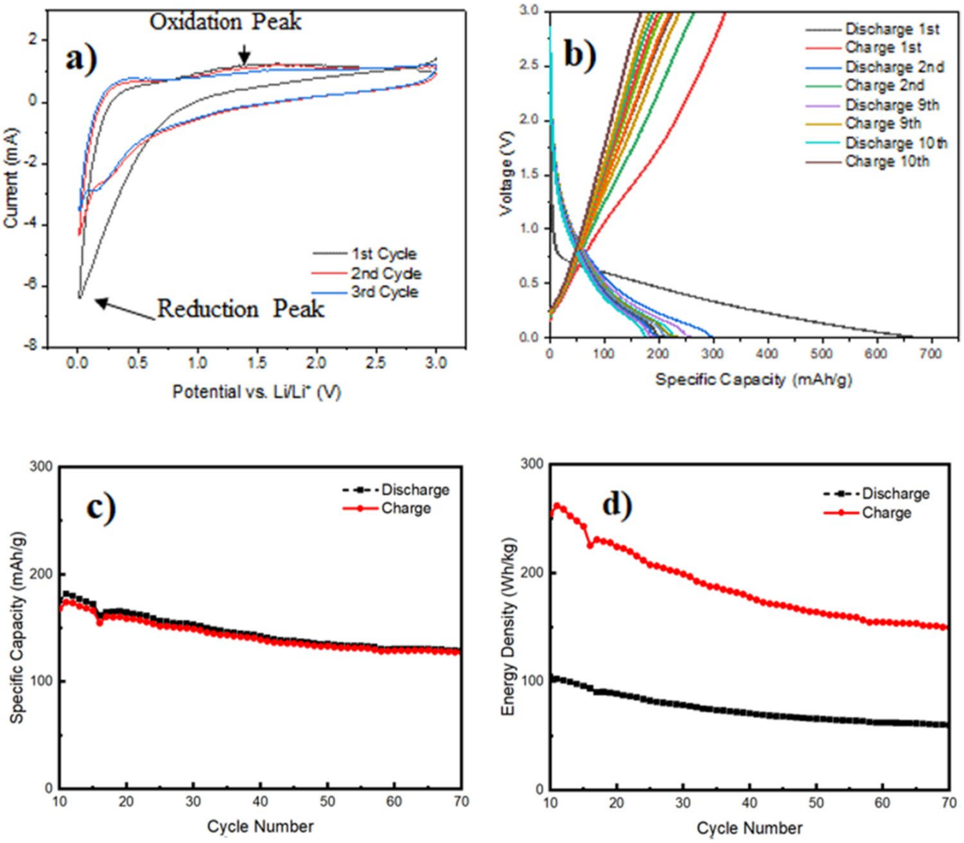

Fig. 5 Electrochemical performance of synthesized rGO. **a** CV of cycles 1–3 at a scan rate of 0.2 mV/s from 0.01 to 3.00 V, **b** discharge/charge curves of the first 10 cycles at 100 mA/g, **c** cyclic stability at 100 mA/g, and **d** energy density measurement at 100 mA/g

The discharge–charge profiles of the first 10 cycles of the synthesized rGO as shown in Fig. 5b, were obtained at a current density of 100 mA/g with a potential window of 0.01–3.00 V. The resulting discharge/charge profiles were consistent with the CV, where an enormous reduction in specific capacity can be observed from the first to the second and subsequent cycles. The initial discharge/charge capacity of the synthesized rGO was 665 mAh/g and 321 mAh/g, with a Coulombic efficiency of 48.3%. The first cycle capacity loss or irreversible capacity was caused by the SEI formation, which is common in carbon-based materials [30]. After 10 cycles, the Coulombic efficiency increases to 95.5%, with a discharge/charge capacity of 176 mAh/g and 168 mAh/g, respectively. This specific value of Coulombic efficiency suggests that capacity reversibility increases due to the decrease in SEI formation and lithium-ion plating activity after the initial cycle. Furthermore, the discharge and charge curves tend to overlap after the first cycle, indicating that the lithiation/de-lithiation process is relatively stable.

The cyclic stability of the synthesized rGO anode was studied for 70 cycles as shown in Fig. 5c at 100 mA/g with a potential window of 0.01 to 3.00 V. After 70 cycles, its discharge capacity is maintained at 129 mAh/g, which is 17.5% of the initial discharge capacity. Capacity retention from initial discharge capacity after 10, 20, 30, 40, 50, and 60 cycles were 176 (26.5%), 164 (24.7%), 153 (23.0%), 142 (21.4%), 135 (20.3%), and 130 (19.5%) mAh/g, respectively. The huge loss in discharge capacity from the initial to the 10th cycle is mainly due to SEI formation. After the 10th cycle, the capacity retention of the capacitance tends to stabilize as shown in Fig. 5c, indicating good cycle performance of the synthesized rGO anode. Figure 5d shows the trends of the discharge/charge energy density of the anodes for 70 cycles. It was observed that the synthesized rGO anode provided the highest energy density of 224 Wh/kg, higher than the theoretical energy density of graphite (200–210 Wh/kg).

In addition, the synthesized rGO anode also exhibits a charge energy density of up to 485 Wh/kg. In contrast, the minimum discharging and charging energy density is 60 and 145 Wh/kg, respectively. The calculated maximum discharge energy density of the synthesized rGO was 994 Wh/kg, which is significantly higher than the actual experimental result of 224 Wh/

kg. This situation arose due to the voltage change experienced by the graphene anode half-cell between the 0.00 and 3.00 V potential window during cycling activity. From the higher calculated energy density, it can be concluded that the synthesized rGO is discharged at a lower voltage than the midpoint voltage of 1.495 V on average. From the initial (maximum) discharge-specific capacity, the C-rate of the initial discharge cycle was calculated to be 0.15 C. By subjecting the synthesized rGO anode half-cell to a current density of 100 mA/g, the synthesized rGO electrode took about 6.67 h to discharge at a discharge current of 1.61 × 10^{-3} A. The low C-rate at the electrochemical measurement of battery electrode testing is common to ensure the most accurate capacity measurement can be achieved by eliminating stresses at a high discharge–charge rate that could be put on the cell.

3.2.2 *Industry's graphene*

The electrochemical performances of the industry's graphene are shown in Fig. 6. The CV profiles of the industry's graphene are shown in Fig. 6a. The CV measurements were carried out in the potential window from 0.01 to 3.00 V against the Li/Li^+ reference electrode with a scanning rate of 0.2 mV/s. Similar to the synthesized rGO, a large irreversible reduction current can be observed in the CV of industry's graphene between the first and the second/third cycle, which is mainly caused by the irreversible lithium-ion intercalation during the cathodic scan. The first cathodic scan shows a broad reduction peak at 0.3 V, which corresponds to the SEI formation on the industry's graphene surface and the reaction of the lithium-ion with the oxygen-containing groups of the industry's graphene. The reduction peak shifted to 0.2 V in the subsequent cycles indicating that the reduction process takes place at a lower potential after the initial cycle. The first anodic scan showed three broad oxidation peaks at 1.2 V, 1.7 V and, 2.4 V. The anodic scan for the second and third cycles shows a broader and less intense oxidation peak for the subsequent cycle, indicating the reaction of the active material with indicates electrolyte decreases as the CV measurement progresses [31].

At a current density of 100 mA/g and a potential window of 0.01 to 3.00 V, the discharge/charge profiles of the first 10 cycles of industry's graphene, as shown in Fig. 6b were obtained by galvanostatic discharging

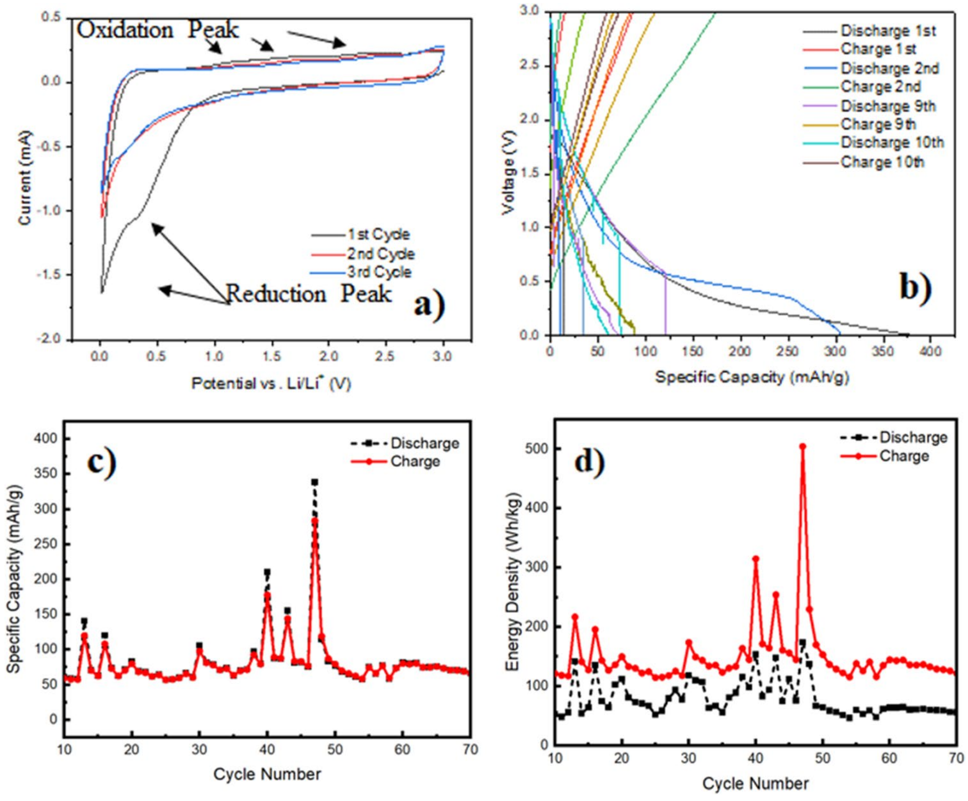

Fig. 6 Electrochemical performance of industry's graphene. **a** CV of cycles 1–3 at a scan rate of 0.2 mV/s from 0.01 to 3.00 V, **b** discharge/charge curves of the first 10 cycles at 100 mA/g, **c** cyclic stability at 100 mA/g, and **d** energy density measurement at 100 mA/g

and charging the half-cell. The discharge/charge profiles show an unstable curve with a lot of noise, especially during the discharging cycles. The industry's graphene showed a significant drop in discharge and charge-specific capacity between each cycle. The initial discharge/charge capacity recorded for the industry's graphene was 377 mAh/g and 86 mAh/g, with a Coulombic efficiency of 22.8%. The low Coulombic efficiency was due to SEI formation, leading to capacity loss and irreversible lithium-ion intercalation. After 10 cycles, the Coulombic efficiency increases to 96.7%, but with a low discharge/charge capacity of only 61 and 59 mAh/g. The increase in capacity reversibility, reflected in the high Coulombic efficiency, suggests less SEI formation after the first cycle. However, the lithiation/de-lithiation process is unstable in the industry's graphene, as shown by the spacious and jagged discharge/charge curve in Fig. 6b.

The cycling performance of industry's graphene as shown in Fig. 6c was tested for 70 cycles at 100 mA/g within 0.01 to 3.00 V. The industry's graphene anode retains 17.5% of its initial discharge capacity after 70 cycles with a capacity of 66 mAh/g. The resulting capacity retention of the industry's graphene after 10, 20, 30, 40, 50 and 60 cycles were 61 (16.2%), 83 (22.0%), 106 (28.1%), 210 (55.7%), 68 (20.8%), and 80 (17.5%) mAh/g, respectively. The industry's graphene shows poor cyclic stability with huge fluctuations in capacity retention recorded for the 70 cycles as shown in Fig. 6c, which agrees well with the discharge/charge curve. This condition could be attributed to the small d-spacing of the industry's graphene of 3.52 Å as analyzed from the XRD pattern, which increases the diffusion energy barrier, leading to unstable lithium-ion diffusion [32]. The recorded discharge/charge energy density of industry's graphene is shown in Fig. 6d. The evaluation of 70 cycles was obtained at a current density of 100 mA/g and a potential window of 0.01 to 3.00 V. The trends in unstable discharge/charge energy density are consistent with the cyclic stability trends because the energy density measurement reflects the discharge/charge capacity with the addition of the voltage consideration. Unfortunately, this is a very unstable system, and it is very unusual for the capacity of a cell/s to fluctuate so much. Aside from the question of material structure, this usually indicates a problem with the cell design or a problem with the test conditions.

It can be observed that the industry's graphene exhibited the highest discharge energy density (second cycle) of 201 Wh/kg at a current density of 100 mA/g. The maximum charge capacity was 505 Wh/kg, while the recorded minimum discharge and charge energy densities were 18 and 28 Wh/kg, respectively. The calculated peak discharge energy density (second cycle) shows a higher value than the experimental value, 454 Wh/kg versus 201 Wh/kg. Thus, the synthesized rGO was subjected to a voltage below the nominal/midpoint voltage of 1.495 V for most of the discharge time. The C-rate of the first discharge cycle for the industry's graphene was set at 0.27 C based on the initial (maximum) discharge-specific capacity. When the industry's graphene anode half-cell was exposed to a current density of 100 mA/g, the graphene electrode discharged in about 3.70 h at a discharge current of 0.22×10^{-3} A, which is a faster and higher discharge current than the synthesized rGO. In the electrochemical measurement of battery electrode testing, a low C-rate is often used to ensure a consistent capacitance reading.

3.2.3 *Commercial rGO*

The electrochemical performances of the commercial rGO are shown in Fig. 7. The scan rate of 0.2 mV/s with a potential window of 0.01 to 3.00 V versus Li/Li^+ was used to measure the cyclic voltammogram (CV) as shown in Fig. 7a, consistent with the other two samples. The difference obtained in the CV of commercial rGO in the first cycle curve compared to the second and third cycle is similar to the other two samples, with a significant irreversible reduction current resulting from irreversible lithium-ion intercalation. The CV curves show scattered sharp and broad reduction and oxidation peaks over the three cycles of CV measurement of the commercial rGO anode. On the first cathodic scan, a prominent sharp reduction peak can be observed at 1.8 V with a broad reduction peak at 0.6 and 0.3 V, and other less obvious peaks. This condition indicates the formation of SEI and a chemical reaction between the active material and the lithium-ion taking place across the cathodic voltage of 0.3 V to 1.8 V. The second and third cathodic scans show the presence of a scattered reduction peak similar to the first cycle, indicating the continuation and presence of SEI formation activities after the initial cycle [33]. The first anodic scan shows a sharp and broad oxidation peak at 2.0 and 2.2 V and other smaller peaks between 1.9 and 2.2 V.

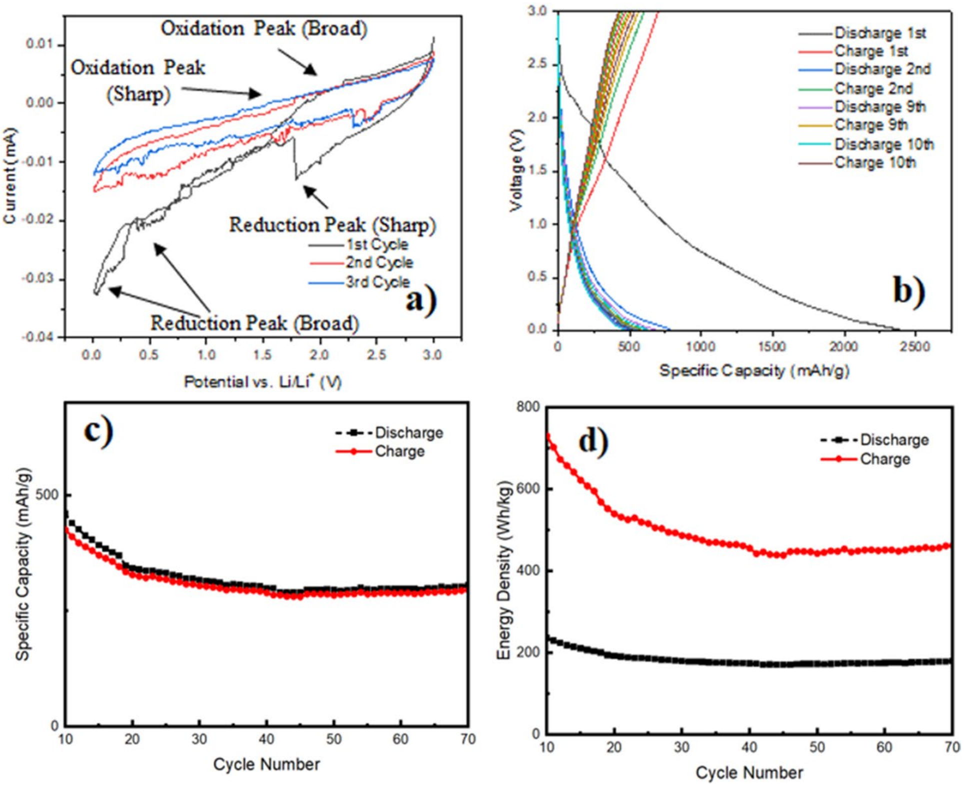

Fig. 7 Electrochemical performance of commercial rGO. **a** CV of cycles 1–3 at a scan rate of 0.2 mV/s from 0.01 to 3.00 V, **b** discharge/charge curves of the first 10 cycles at 100 mA/g, **c** cyclic stability at 100 mA/g, and **d** energy density measurement at 100 mA/g

The second and third anodic scans show no apparent oxidation peak, consistent with the stabilization of lithium-ion intercalation reversibility after the initial cycle. The discharge/charge curves of the initial 10 cycles of the commercial rGO are shown in Fig. 7b, performed at 100 mA/g with a potential window of 0.01 to 3.00 V. The massive drop in discharge capacity from the initial cycle to the subsequent cycles is consistent with the CV where a significant irreversible reduction current was observed. The initial discharge/charge capacity of the commercial rGO anode was as high as 2383 and 697 mAh/g with a Coulombic efficiency of 29.2%. The huge capacity loss is mainly due to the SEI formation observed in the scattered reduction peaks in the CV curves. After 10 cycles, the Coulombic efficiency increases to 92.6%, with a discharge/charge capacity of 460 and 426 mAh/g, indicating a decrease in SEI formation and lithium-ion activities in the tenth cycle. The discharge and charge curves also tend to overlap after the initial cycle, indicating a stable lithiation/de-lithiation process.

The cyclic performance of the commercial rGO can be observed from the cyclic stability trends in Fig. 7c. The commercial rGO anode delivers a discharge capacity of 305 mAh/g after 70 cycles and retains 12.8% of the initial discharge capacity. The remaining capacity from the initial discharge after 10, 20, 30, 40, 50, and 60 cycles were 460 (19.3%), 342 (14.4%), 317 (13.3%), 299 (12.5%), 296 (12.4%), and 298 (12.5%) mAh/g, respectively. The commercial rGO anode exhibits high cyclic stability as shown by the cycling trends in Fig. 7c, with an almost constant percentage of capacity retention after 40 cycles. The low percentage of detected capacity retentions is mainly due to the huge loss of irreversible lithium-ion intercalation, as discussed in the CV and discharge/charge profiles. The discharge/charge energy density trends for the commercial rGO are shown in Fig. 7d and were recorded at 100 mA/g between 0.01 and 3.00 V. The commercial rGO delivers the maximum energy density of up to 1866 Wh/kg, the maximum charging energy density is up to 1180 Wh/kg. It also shows a stable trend in discharge/charge energy density, consistent with the stable cyclic performance of the commercial rGO anode. The recorded minimum discharge energy density was 171 Wh/kg while the minimum charge energy density was 438 Wh/kg. The maximum calculated energy density of the commercial rGO is up to 3563 Wh/kg based on the capacity value of the first discharge cycle, showing the potential of the commercial rGO anode to deliver an extremely high energy density when operated at a constant nominal voltage of 1.495 V during the discharge cycle. However, the resulting experimental energy density of 1866 Wh/kg is more in line with real application where the cell is powering the devices in a range of voltages rather than a constant voltage. The calculated C-rate of the commercial rGO anode is the lowest to date of all three graphene anode samples at just 0.04 C, which corresponds to a discharged time of about 25 h for the initial discharge cycle. This condition is strongly influenced by the weight of the coated commercial rGO electrode, which is only 0.0009 g due to its light and fluffy properties thanks to the effective exfoliation, that creates large pores between the graphene nanosheets as shown in the SEM analysis. A smaller C-rate allows a more stable current to be delivered to the anode relative to its weight, so an accurate measurement of capacitance can be achieved.

3.3 The summary of the electrochemical performance of graphene anode materials

Electrochemical performance evaluation results of all three graphene anode samples were extracted from each test and presented in Table 3. In terms of specific capacity, the commercial rGO turned out to provide the highest discharge/charge capacity among all samples during the first and tenth cycle. This state is attributed to the highly stacked graphene nanosheets with large-pore morphological structure of commercial rGO that provide space for lithium-ion intercalation. The synthesized rGO shows the highest capacity reversibility during the first cycle and records 48.3% of the Coulombic efficiency, indicating the lowest formation of SEI and lithium-ion plating activity in the first cycle. However, after 10 cycles of discharge and charge, the industry’s graphene reversed the highest capacitance of any sample, recording a 96.7% coulombic efficiency.

Among all the samples, the synthesized rGO retained the highest discharge capacity after 70 cycles, which is 19.4% of the discharge capacity of the initial cycle. The industry’s graphene follows this condition with a capacity retention of 17.5%, while commercial rGO boasts the lowest capacity retention of 12.8%. This condition shows that the commercial rGO suffers the most from SEI formation during the 70 cycles compared to the synthesized rGO and the industry’s graphene. However, in terms of cyclic stability, the commercial rGO shows the most stable cyclic performance, which can be seen from the almost constant capacity

Table 3 Electrochemical performance summarization of graphene anode samples

Electrochemical performance evaluation			Samples		
			Synthesized rGO	Industry’s graphene	Commercial rGO
GCD (specific capacity)	1st Cycle	Discharge capacity (mAh/g)	665	377	**2383**
		Charge capacity (mAh/g)	321	86	**697**
		Coulombic efficiency (%)	**48.3**	22.8	29.2
	10th Cycle	Discharge capacity (mAh/g)	176	61	**460**
		Charge capacity (mAh/g)	168	59	**426**
		Coulombic efficiency (%)	95.5	**96.7**	92.6
Cyclic stability	Capacity retention (%)	After 10 cycles	**26.5**	16.2	19.3
		After 20 cycles	**24.7**	22.0	14.4
		After 30 cycles	23.0	**28.1**	13.3
		After 40 cycles	21.4	**55.7**	12.5
		After 50 cycles	20.3	**20.4**	12.4
		After 60 cycles	19.5	**21.5**	12.5
		After 70 cycles	**19.4**	17.5	12.8
Energy density	Discharge	Maximum (Wh/kg)	224	201	**1866**
		Minimum (Wh/kg)	60	18	**171**
	Charge	Maximum (Wh/kg)	485	505	**1180**
		Minimum (Wh/kg)	145	28	**438**

The highest values obtained by the examined samples for each analyzed parameter aregiven in bold retention recorded after 40 cycles. The synthesized rGO exhibited the second-best cyclic performance, while the industry's graphene exhibited unstable cyclic performance, as evidenced by the huge swings in cycling trends. The energy density data shows that the commercial rGO has the highest discharging and charging energy density of 1866 Wh/kg and 1180 Wh/kg.

The synthesized rGO recorded the second-highest discharge energy density at 224 Wh/kg. In comparison, the industry's graphene has the lowest discharge energy density of 201 Wh/kg of all three graphene samples. However, the charging energy density of industry's graphene is slightly higher than that of synthesized rGO at 505 Wh/kg compared to 485 Wh/kg, respectively. In terms of minimum energy density, industry's graphene recorded the lowest discharging and charging energy density at 18 and 28 Wh/kg, while the minimum discharging and charging energy density of industry's graphene is higher at 60 and 145 Wh/kg. Table 4 shows the comparison of this and other work on the specific capacity results of graphene-based anode for lithium-ion batteries. It turned out that this work resulted, among other things, in the significantly higher capacitance value, thus confirming that the electrode is suitable for the realization of advanced anodes in LIB technology.

In summary, Graphene-based anodes have been successfully fabricated by the manual electrode fabrication method. The reduced graphene oxide (rGO) was synthesized from the graphite flakes via the top-down chemical synthesis method. The anodes were manufactured manually with the composition active material, acetylene black and PVDF in a weight ratio of 8:1:1. Raman spectroscopy revealed that all three graphene samples exhibited D- and G-band peaks, confirming the presence of graphitic structure in all samples. The I_D/I_G ratio shows that the synthesized rGO has the highest defect density among all three samples due to the chemically exfoliating process. Characterization of the morphological properties revealed highly ordered stacks of graphene nanosheets present in the commercial rGO, while the surface of the synthesized rGO is wrinkled and crumpled due to an ineffective exfoliation process. XRD patterns showed that the synthesized rGO is more crystallized, followed by commercial rGO, and the industrial graphene is the most amorphous of the three.

Electrochemical tests revealed a specific capacity and energy density of up to 2383 mAh/g and 1866 Wh/kg was estimated for commercial rGO. An effective graphene exfoliation turns out to be very crucial for the electrochemical performance of the anode in the lithium-ion battery. As shown in the SEM image of commercial rGO, the porous morphology provides space for lithium-ion intercalation and is very beneficial for increasing specific capacity and energy density. Up to 19.4% of the capacity was retained after 70 cycles as shown by the synthesized rGO. The SEI formation and the irreversible lithium-ion intercalation process during the battery cycling are believed to significantly affect the coulombic efficiency and capacity retention of carbon-based anodes. The large irreversible reduction current significantly reduced the performance of the anode. The uniqueness of rGO as graphene derivatives has proven to be a great anode material as there is still more room to fully utilize and improve rGO's potential. Therefore, this study offers tremendous opportunities for scientists and engineers to further explore the anode materials for high-performance lithium-ion batteries to overcome the low capacity of the widely used graphite.

For the implications of the results, rGO offers numerous advantages, including higher theoretical capacity, and structural adaptability, all while remaining cost-effective and eco-friendly. However, it's important to consider some potential drawbacks, such as limited research on rGO in LFP batteries, lower stability compared to graphite, and a possible lower Coulombic efficiency. Ultimately, while rGO holds

Table 4 Comparison of specific capacity of graphene-based anode in LIB with other works

No.	Sample	Anode type	Specific capacity (mAh/g)	References
1	Azam et al.	Commercial rGO	2383	This work
2	Tang et al.	VPO_4@C/graphene	1074	[34]
3	Guo et al.	Graphene/SnO_2	1109	[35]
4	Fu et al.	rGO-thermal reduction	578	[36]
5	Gao et al.	MOF/SnO_2/Graphene	450	[37]
6	Idrees et al.	SiBCN/NSGs composite	785	[38]
7	Zing et al.	Porous graphene	770	[39]
8	Jiao et al.	P/CNG composite	2522	[40]

promise as a sustainable energy storage solution, further research is necessary to fully evaluate its benefits and drawbacks. Besides, we have identified certain limitations that warrant consideration for future research endeavours. Firstly, our study primarily focused on rGO-based anode materials, and while this provided valuable insights into their electrochemical performance, a comparative analysis with other anode materials would enhance our understanding of rGO's distinct advantages and limitations.

Furthermore, our investigation mainly examined the electrochemical aspects and structural characterizations, leaving room to explore other critical aspects such as thermal stability, mechanical properties, and the interface between the anode and electrolyte. Additionally, the scalability and cost-effectiveness of integrating rGO into lithium-ion batteries should be investigated to ensure its practicality for large-scale battery applications. Lastly, incorporating environmentally friendly synthesis methods for rGO production could be explored to align with sustainability objectives. Future research should also aim to optimize the synthesis process to improve the overall performance of rGO-based anode materials, considering various factors like precursor types, reduction methods, and doping strategies. These advancements will undoubtedly contribute to the broader goal of enhancing lithium-ion battery technologies.

4 Conclusions

This study successfully fabricated graphene-based anodes using the manual electrode fabrication method. The reduced graphene oxide (rGO) was synthesized from graphite flakes via the top-down chemical synthesis method. The study found that the synthesized rGO has the highest defect density among all three samples due to the chemically exfoliating process. The commercial rGO has the highest discharging and charging energy density of 1866 Wh/kg and 1180 Wh/kg, respectively. The synthesized rGO retained the highest discharge capacity after 70 cycles, while the commercial rGO boasts the lowest capacity retention. The study suggests that effective graphene exfoliation is crucial for the electrochemical performance of the anode in the lithium-ion battery. The porous morphology of commercial rGO provides space for lithium-ion intercalation and is very beneficial for increasing specific capacity and energy density. However, the SEI formation and the irreversible lithium-ion intercalation process during the battery cycling significantly affect the coulombic efficiency and capacity retention of carbon-based anodes. The study concludes that the uniqueness of rGO as graphene derivatives has proven to be a great anode material, and there is still more room to fully utilize and improve rGO's potential. Further research is needed to optimize the synthesis and performance of rGO-based anodes for high-performance lithium-ion batteries to overcome the low capacity of the widely used graphite.

Acknowledgements

Authors are grateful to Fakulti Kejuruteraan Pembuatan and Universiti Teknikal Malaysia Melaka for the facilities support and UTeM Zamalah Scheme for PhD support of Nur Ezyanie Safie.

Author contributions

Conceptualization, MAA and AT; methodology, CCK and NES; validation, MAA; formal analysis, CCK, MFAA, and MNFMS; investigation, CCK, MFAA, and MNFMS; resources, MAA; data curation, MAA and NES; writing—original draft preparation, MAA, and CCK; writing—review and editing, NES and AT; visualization, MAA; supervision, MAA; project administration, MAA; funding acquisition, MAA. All authors have read and agreed to the published version of the manuscript.

Data availability

The datasets generated during and/or analyzed during the current study are available from the corresponding author on reasonable request.

Declarations

Conflict of interest The authors declare no conflict of interest.

References

1. M.A. Azam, N.E. Safie, A.S. Ahmad, N.A. Yuza, N.S. Zulkifli, J. Energy Storage **33**, 102096 (2021)
2. L.W. Tack, M.A. Azam, R.N.A.R. Seman, J. Phys. Chem. A **121**, 2636–2642 (2017)
3. M.A. Azam, N.S. Ramli, N.A. Nor, T.I. Nawi, Int. J. Energy Res. **45**, 8335–8346 (2021)
4. T. Jiang, F. Bu, X. Feng, I. Shakir, G. Hao, Y. Xu, ACS Nano **11**, 5140–5147 (2017)
5. Y. Wu, W. Wang, J. Ming, M. Li, L. Xie, X. He, J. Wang, S. Liang, Y. Wu, Adv. Funct. Mater. **29**, 1805978 (2019)
6. J. Asenbauer, T. Eisenmann, M. Kuenzel, A. Kazzazi, Z. Chen, D. Bresser, Sustain. Energy Fuels **4**, 5387–5416 (2020)
7. R.P. Luo, W.Q. Lyu, K.C. Wen, W.D. He, J. Electron. Sci. Technol. **16**, 57–68 (2018)
8. X. Han, L. Lu, Y. Zheng, X. Feng, Z. Li, J. Li, M. Ouyang, ETransportation **1**, 100005 (2019)
9. S.K. Marka, V.V.H. Peruswamula, V.S.S.S. Vadali, *Nanocarbon Electrochemistry* (Wiley, New York, 2019), pp.85–121
10. J. Lu, Z. Chen, F. Pan, Y. Cui, K. Amine, Electrochemical Energy Reviews **1**, 35–53 (2018)
11. N.E. Safie, M.A. Azam, M.F. Aziz, M. Ismail, Int. J. Energy Res. **45**, 1347–1374 (2021)
12. R.N.A.R. Seman, M.A. Azam, M.H. Ani, Nanotechnology **29**, 502001 (2018)
13. L. Lin, H. Peng, Z. Liu, Nat. Mater. **18**, 520–524 (2019)
14. N.E. Safie, M.A. Azam, A.I.M.S. Mater, Sci. **9**, 617–627 (2022)
15. P. Puech, M. Kandara, G. Paredes, L. Moulin, E. Weiss-Hortala, A. Kundu, N. Ratel-Ramond, J.M. Plewa, R. Pellenq, M. Monthioux **5**, 69 (2019)
16. M.A. Azam, M.F. Aziz, N.N. Zulkapli, G. Omar, R.F. Munawar, M.S. Suan, N.E. Safie, Diam. Relat. Mater. **104**, 107767 (2020)
17. Z. Li, R. Wang, S. Wu, Z. Xue, D. Zhu, J. Zou, X. Li, Carbon **184**, 721–727 (2021)
18. E.F. Sheka, Y.A. Golubev, N.A. Popova, Nanomaterials **10**, 2021 (2020)
19. P. Vinchon, X. Glad, G. Robert Bigras, R. Martel, L. Stafford, Nat. Mater. **20**, 49–54 (2020)
20. W.M.A. El Rouby, RSC Adv. **5**, 66767–66796 (2015)
21. G.A. McQuade, A.S. Plaut, A. Usher, J. Martin, Appl. Phys. Lett. **118**, 203101 (2021)
22. S. Mann, R. Kumar, V.K. Jindal, RSC adv. **7**, 22378–22387 (2017)
23. H.G. Rasheev, R.B. Araujo, A. Tadjer, P. Johansson, J. Mater. Chem. A **8**, 14152–141561 (2020)
24. C. Xiong, B. Li, X. Lin, H. Liu, Y. Xu, J. Mao, C. Duan, T. Li, Y. Ni, Compos. B Eng. **165**, 10–46 (2019)
25. G. Ali, A. Mehmood, H.Y. Ha, J. Kim, K.Y. Chung, Sci. Rep. **7**, 1–8 (2017)
26. S. Abbas, A. Abbas, N.M. Bhattarai, N. Latiff, A.N. Wai, T.M. Phan, Lim, J. Power. Sources **488**, 229411 (2021)
27. E. Sohouli, E.M. Khosrowshahi, M. Ghalkhani, K. Eskandari, M. Aghaei, M. Rahimi-Nasrabadi, A. Sobhani-Nasab, H. Banafshe, E.K. Nasrabadi, Surf. Interfaces **30**, 101943 (2022)
28. S. Liang, K. Yu, Y. Li, C. Liang, Mater. Res. Express **7**, 015021 (2020)
29. K. Rana, S.D. Kim, J.H. Ahn, Nanoscale **7**, 7065–7071 (2015)
30. G. Yuan, G. Wang, H. Wang, J. Bai, J. Alloys Compd. **660**, 62–72 (2016)
31. S.K. Pandey, S. Sachan, S.K. Singh, Mater. Sci. Energy Technol. **2**, 676–686 (2019)
32. B. Xu, M.S. Wu, G. Liu, C.Y. Ouyang, J. Appl. Phys. **111**, 124325 (2012)
33. B. Jin, F. Gao, Y.F. Zhu, X.Y. Lang, G.F. Han, W. Gao, Q. Jiang, Sci. Rep. **6**, 19317 (2016)
34. L.B. Tang, B. Xiao, C.S. An, H. Li, Z.J. He, J.C. Zheng, Ceram. Int. **44**, 14432–14438 (2018)
35. Q. Guo, S. Chen, X. Qin, Mater. Lett. **119**, 4–7 (2014)
36. C. Fu, G. Zhao, H. Zhang, S. Li, Int. J. Electrochem. Sci. **8**, 6269–6280 (2013)
37. C. Gao, Z. Jiang, P. Wang, L.R. Jensen, Y. Zhang, Y. Yue, Nano Energy **74**, 104868 (2020)
38. M. Idrees, S. Batool, J. Kong, Q. Zhuang, H. Liu, Q. Shao, N. Lu, Y. Feng, E.K. Wujcik, Q. Gao, T. Ding, Electrochim. Acta **296**, 925–937 (2019)
39. B. Xing, H. Zeng, G. Huang, C. Zhang, R. Yuan, Y. Cao, Z. Chen, J. Yu, J. Alloys Compd. **779**, 202–211 (2019)
40. X. Jiao, Y. Liu, T. Li, C. Zhang, X. Xu, O.O. Kapitanova, C. He, B. Li, S. Xiong, J. Song, ACS Appl. Mater. Interfaces **11**, 30858–30864 (2019)